



# Stabilizing intermediates and optimizing reaction processes with N doping in Cu<sub>2</sub>O for enhanced CO<sub>2</sub> electroreduction

Chunliu Yan<sup>a</sup>, Wen Luo<sup>b</sup>, Huimin Yuan<sup>b</sup>, Guiyu Liu<sup>b</sup>, Rui Hao<sup>b</sup>, Ning Qin<sup>b</sup>, Zhiqiang Wang<sup>b</sup>, Kun Liu<sup>b</sup>, Zhenyu Wang<sup>b</sup>, Dehu Cui<sup>a,\*</sup>, Zhuofeng Hu<sup>c,\*</sup>, Yangchun Lan<sup>a,\*</sup>, Zhouguang Lu<sup>b,\*</sup>

<sup>a</sup> School of Microelectronics, Southern University of Science and Technology, Shenzhen 518055, PR China

<sup>b</sup> Department of Materials Science and Engineering, Shenzhen Key Laboratory of Interfacial Science and Engineering of Materials, Guangdong-Hong Kong-Macao Joint Laboratory for Photonic-Thermal-Electrical Energy Materials and Devices, Southern University of Science and Technology, Shenzhen 518055, PR China

<sup>c</sup> School of Environmental Science and Engineering, Guangdong Provincial Key Laboratory of Environmental Pollution Control and Remediation Technology, Sun Yat-sen University, Guangzhou 510275, PR China

## ARTICLE INFO

### Keywords:

CO<sub>2</sub> electroreduction  
Intermediates adsorption  
Reaction kinetic  
Nitrogen doping copper oxides  
In-situ surface enhanced Raman spectroscopy (SERS)

## ABSTRACT

Appropriate adsorption strength and modes of intermediates on catalysts and the reaction kinetic energy barrier directly determine the selectivity and productivity of final products during CO<sub>2</sub> electroreduction. This work systematically reveals the mechanisms for enhanced CO<sub>2</sub> electroreduction on nitrogen-doped Cu<sub>2</sub>O (N-Cu<sub>2</sub>O) catalyst by in-situ surface enhanced Raman spectroscopy (SERS) and theoretical calculation. The introduction of N into Cu<sub>2</sub>O can significantly enhance the CO<sub>2</sub> adsorption capacity, binding strength of key intermediates and increase the local pH value, resulting in two-fold enhancement of CO and C<sub>2</sub>H<sub>4</sub> production as compared to bare Cu<sub>2</sub>O. Meanwhile, the protonation step is promoted, making the formation of COOH<sup>•</sup> quickly and earlier. Therefore, the adsorbed CO<sub>2</sub><sup>•-</sup> intermediate formation is produced more rapidly, and the rate-determining step is transferred, continually facilitating the electroreduction of CO<sub>2</sub>. This study is inspiring in designing high-performance electrocatalysts for CO<sub>2</sub> reduction.

## 1. Introduction

Conversion CO<sub>2</sub> into chemical products is a promising strategy to close the anthropogenic carbon cycle, and relieve environmental problems [1]. From the perspective of sustainable energy production, electrochemical CO<sub>2</sub> reduction reaction (CO<sub>2</sub>RR) has gained wide attention from researchers [2,3]. However, the high stability of CO<sub>2</sub> and multi-step transfer kinetics of the reaction lead to large overpotential, low product selectivity and energetic efficiency, seriously blocking the practical use [4]. Over the past few decades, researchers have investigated various kinds of electrocatalysts for electrochemical reduction CO<sub>2</sub> into value-added chemical products in aqueous solution. However, none of them are stable and efficient for the industrial-level applications [5–7]. Tremendous efforts have been devoted to optimize the catalyst's structure via surface modifications, alloying, and heteroatom doping [8–12]. Heteroatom doping is an effective strategy for modifying metal or oxygen vacancies in catalysts. It can tune the intermediates' binding strength, thus boosting CO<sub>2</sub> conversion. Copper and copper-based materials have also attracted considerable attention as the most active

candidates for converting CO<sub>2</sub> to valuable chemicals [13–16]. After heteroatom doping, the electronic structure of copper and copper-based materials is optimized, it is beneficial for CO<sub>2</sub>RR [17,18]. Zhuang et al. introduced S atom to Cu catalyst and adjusted Cu vacancies to steer the post-C-C coupling selectivity and produce multi-carbon alcohols [19]. Catalyst with Cu vacancies delivered six-fold enhancement for alcohols compared with those without Cu vacancies. Besides, Wan et al. have synthesized B-doped CuO nanobundles (boron ~0.49 wt%), generating oxygen vacancies, thereby enhancing the CO<sub>2</sub> adsorption capacity on the catalyst surface [20]. Theoretically, the Nitrogen (N) element as an oxide dopant can also cause oxygen vacancies, N with a pair of electron is expected to improve CO<sub>2</sub> adsorption ability and enhance the binding energy of key intermediates during the process of CO<sub>2</sub>RR in aqueous solution [21,22]. N-doping carbon catalysts have attracted extensive attention because defective N sites can facilitate high activity for converting CO<sub>2</sub> to CO [23–25]. However, the effects of N doping on modulating the electrochemical CO<sub>2</sub>RR activity and selectivity over copper oxides have been rarely explored, and the mechanism still remains unclear.

\* Corresponding authors.

E-mail addresses: [cuidh@sustech.edu.cn](mailto:cuidh@sustech.edu.cn) (D. Cui), [huzhf8@mail.sysu.edu.cn](mailto:huzhf8@mail.sysu.edu.cn) (Z. Hu), [lanyc@mail.sustech.edu.cn](mailto:lanyc@mail.sustech.edu.cn) (Y. Lan), [luzg@sustech.edu.cn](mailto:luzg@sustech.edu.cn) (Z. Lu).

<https://doi.org/10.1016/j.apcatb.2022.121191>

Received 21 October 2021; Received in revised form 19 January 2022; Accepted 4 February 2022

Available online 8 February 2022

0926-3373/© 2022 Elsevier B.V. All rights reserved.

Actually, short existence time and relatively weak detectable signals of reaction intermediates make it difficult to analyze the reaction mechanisms during CO<sub>2</sub>RR. Therefore, it is highly desirable to get insight into surface species during CO<sub>2</sub> reduction. Thanks to the development of in-situ spectroscopic techniques, such as in-situ infrared (IR) spectroscopy, in-situ X-ray absorption spectroscopy (XAS) and in-situ SERS, which can provide real-time information of the absorbed reaction intermediates on catalyst's surface [26]. In-situ SERS works as a fingerprint spectrum collector with high sensitivity is an efficient technology to monitor solid-liquid interface and surface intermediates during CO<sub>2</sub>RR in aqueous solution [27,28]. An et al. have reported time-resolved SERS to reveal dynamic \*CO intermediates during CO<sub>2</sub>RR on the copper surface [29]. Hence, in-situ SERS is expected to reveal the intrinsic function of the N element by analyzing different intermediates adsorption modes and strength on the catalyst's surface.

Herein, in-situ SERS measurement and DFT calculation have been utilized to monitor the CO<sub>2</sub> electroreduction on Cu<sub>2</sub>O and N-Cu<sub>2</sub>O catalysts and unravel the mechanisms for the enhanced electroreduction performance of N-doped Cu<sub>2</sub>O. Two kinds of carboxyl intermediates (\*COOH and OC\*O\*) and \*CO adsorption states are probed, which are critical intermediates for CO, HCOOH, and C<sub>2</sub>H<sub>4</sub> production. Intensities of these peaks are improved about several times stronger and appear under more positive potentials by N doping. That is beneficial for discovering the significant intermediates during the process of CO<sub>2</sub>RR in aqueous solution. Besides, N doping in the Cu<sub>2</sub>O catalyst is proved to increase the CO<sub>2</sub> adsorption capacity and optimize the rate-determining step (RDS) during CO<sub>2</sub>RR. After N-doping, the Tafel plots indicate that the RDS is transferred, which is not restricted to the traditional step (CO<sub>2</sub> + e<sup>-</sup> → CO<sub>2</sub><sup>-</sup>), and simultaneously continues the subsequent step reactions. It tends to produce further reduction products during the procedure of CO<sub>2</sub>RR. Combined with DFT calculation, the function of N doping is profoundly analyzed.

## 2. Experimental section

### 2.1. Catalyst preparation

**Synthesis of Cu<sub>2</sub>O:** Cubic Cu<sub>2</sub>O was synthesized by one-step simple reduction reaction of CuSO<sub>4</sub>. Firstly, CuSO<sub>4</sub>·5H<sub>2</sub>O (1.5 mmol) was dissolved in 100 mL deionized water, then Na<sub>3</sub>C<sub>6</sub>H<sub>5</sub>O<sub>7</sub>·2H<sub>2</sub>O (0.51 mmol) and NaOH (25 mmol) were added into the CuSO<sub>4</sub>·5H<sub>2</sub>O solution respectively, stirring for 5 min to get a homogeneous solution. In addition, ascorbic acid (1.5 mmol) was dissolved in 50 mL deionized water, after mixing uniformly, ascorbic acid solution was dropwise added into the above solution. After keeping stirring vigorously for 40 min under room temperature, the final product was collected by centrifuging and washed with ethanol and deionized water for several times. Finally, the product was dried in oven at 80 °C for 12 h.

**Synthesis of N-Cu<sub>2</sub>O:** For the synthesis of N-Cu<sub>2</sub>O, the as prepared Cu<sub>2</sub>O was annealing at 300 °C for 30 min under NH<sub>3</sub> (99.99%) atmosphere with a heating rate of 5 °C per minutes.

### 2.2. Catalyst characterization

The X-ray powder diffraction (XRD) patterns were conducted by Rigaku smartlab with a Cu Kα radiation. The field emission scanning electron microscopy (SEM) images were obtained by the ZEISS Gemini-300 scanning electron microscope. Transmission electron microscopy (TEM) images, high-resolution TEM images and energy-dispersive X-ray (EDX) spectroscopy were collected by a JEM-2100 transmission electron microscope equipped with EDX analyzer at 200 kV. X-ray photoelectron spectral (XPS) were performed by ES-CALAB 250Xi (Thermo Fischer) with Al Kα excitation source (hν = 1253.6 eV). N<sub>2</sub> sorption and desorption curve were measured at 77 K by Quadrasorb SI. CO<sub>2</sub> adsorption capability test was conducted by Micromeritics ASAP 2460 under room temperature.

### 2.3. Electrochemical measurements and product analysis

The Electrochemically active surface area (ECSA) was performed according to the equation: ECSA = R<sub>f</sub> × S (Eq. 1) where R<sub>f</sub> is the working electrodes' roughness factor, S is the real surface area of oxide electrode, R<sub>f</sub> was gained from the double-layer capacitance of a smooth oxide surface R<sub>f</sub> = C<sub>dl</sub>/60 (μF/cm<sup>2</sup>). The double-layer capacitance (C<sub>dl</sub>) was implemented the capacitive current associated with double-layer charging form the scan rate dependence of Cyclic voltammetry (CV). The potential window of CV was carried out in 0.2–0.1 V (vs. RHE) at various scan rates (10, 20, 50, 70, 100 and 120 mV/s). The C<sub>dl</sub> is determined by plotting the Δj (j<sub>a</sub>-j<sub>c</sub>) at 0.15 V (vs. RHE), where the j<sub>c</sub> and j<sub>a</sub> are the cathodic and anodic current density. The electrochemical measurement was conducted according to the previous report [30]. It was performed via Autolab electrochemical workstation (PGSTAT-302 N, EcoChemie) in H-type electrolysis cell, separated by a Nafion-117 membrane. The three-electrode configuration is composed of working electrode, Pt counter electrode and Ag/AgCl reference electrode (R0302, 3.5 M KCl). And electrolyte is 0.5 M CO<sub>2</sub>-saturated KHCO<sub>3</sub> solution (Sigma Aldrich, Granular, ACS reagent, 99.7%) with a pH of about 6.85. The catalyst (1 mg), deionized water (100 μL), isopropyl alcohol (100 μL) and Nafion solution (2.5 μL, 5 wt%, Fuel Cell Earth) was mixed and then dropwise on a gas diffusion layer (GDL) utilized as working electrode (the geometric area was 1 cm<sup>2</sup>). All cathode potentials were converted to the RHE by the Nernst equation: E(vs RHE) = E(vs Ag/AgCl) + 0.197V + 0.0591V × pH. (Eq. 2) A mass flow controller (LF 400-s/A series) maintained CO<sub>2</sub> (99.999%) flow at 10 SCCM into the cathodic compartment. The gas sample was analyzed using a gas chromatograph (SRI Instruments) equipped with thermal conductivity detector (molecular sieve 5 A column) and flame ionization detector (TM-PLOTU column) argon (99.999%) as carrier gas. The liquid products were quantified by nuclear magnetic resonance (NMR, Bruker Avance III 400 M) spectroscopy. For quantifying the liquid products, 200 μL electrolyte was mixed with 400 μL D<sub>2</sub>O and 100 μL dimethyl sulfoxide (DMSO, 1 mm, Sigma Aldrich, Granular, ACS reagent, 99.9%) as an internal standard.

### 2.4. In-situ Raman spectroscopy test

Raman spectrums were generated by Renishaw (InVia Reflex) Raman spectroscopy equipped with 633 nm wave-length laser and the data was collected by corresponding software (Wire) in the Raman shift from 200 to 2400 cm<sup>-1</sup> at the interval of 0.1 V. For the long-time electrolysis, the spectrum was recorded every 100 s. The Raman electrolysis cell (GaossUnion, China) consisted of three electrodes including counter electrode (Pt wire), reference electrode (Ag/AgCl) and working electrode (Cu<sub>2</sub>O and N-Cu<sub>2</sub>O). The working electrode was prepared with a catalyst-loading of 1 mg/cm<sup>2</sup> on a gas diffusion layer. And the electrolyte is CO<sub>2</sub>-saturated 0.5 M HKCO<sub>3</sub> solution.

### 2.5. Density functional theory methods

Vienna ab initio simulation package (VASP) was used to conduct Density function calculation (DFT) [30,31]. Projector-augmented-wave method with the Perdew-Burke-Ernzerhof GGA functional was applied [32–34]. The electronic convergence limit was set to be 1 × 10<sup>-5</sup> eV [35]. Optimization of atomic coordinates was considered to be converged when Hellmann-Feynman force was smaller than 1 × 10<sup>-2</sup> eV Å<sup>-1</sup>. The Cu<sub>2</sub>O slab consists of 32 Cu atoms and 16 O atoms, while the N-Cu<sub>2</sub>O slab consist of 32 Cu atoms, 15 O atoms and 1 N atom. CO<sub>2</sub> and different intermediates like \*CO and \*COOH are placed on the top of the Cu<sub>2</sub>O substrate. The Brillouin zone integrations were performed with a Gamma-center 2 × 2 × 2 k-point mesh. The vacuum region is about 10 Å in height.

### 3. Results and discussion

#### 3.1. Structural characterization and component analysis

X-ray diffraction (XRD) patterns of as-prepared  $\text{Cu}_2\text{O}$  and N- $\text{Cu}_2\text{O}$  catalysts are shown in Fig. S1, respectively. The sharp and clear diffraction peaks indicate the good crystallinity nature of  $\text{Cu}_2\text{O}$  crystal, which is well-matched with the JCPDS No.05-0667 [36]. After N doping, the diffraction peaks of N- $\text{Cu}_2\text{O}$  are similar to  $\text{Cu}_2\text{O}$ , confirming that no apparent difference between  $\text{Cu}_2\text{O}$  and N- $\text{Cu}_2\text{O}$  catalysts in the crystal structure. The morphology was examined using scanning electron microscopy (SEM). As shown in Fig. 1a, the  $\text{Cu}_2\text{O}$  has cubic structural morphology with a diameter of about 150 nm. The N- $\text{Cu}_2\text{O}$  catalyst retains the cubic morphology, but the surface is rougher than bare  $\text{Cu}_2\text{O}$  with numerous pores (Fig. 1b), favorable for higher  $\text{CO}_2$  absorption capacity on the catalyst surface. High resolution transmission electron microscopy (HRTEM) further validated the nanoscopic characteristic of the  $\text{Cu}_2\text{O}$  and N- $\text{Cu}_2\text{O}$  catalysts. The HRTEM images in Fig. 1c, revealed the successive lattices fringes with a lattice distance of 0.21 nm, corresponding to the (100) plane of  $\text{Cu}_2\text{O}$ . After N-doping, both (100) and (110) facets with an interplanar distance of 0.21 nm and 0.29 nm, respectively have been observed (Fig. 1d) [37]. According to the literature, this structure containing multiple grain-boundaries may bond CO intermediate strongly and promote the production of C<sub>2</sub> products [38]. Energy dispersive X-ray spectroscopy (EDX) mapping images of  $\text{Cu}_2\text{O}$  and N- $\text{Cu}_2\text{O}$  catalysts are displayed in Figs. S2, and 1(f–h). The Cu and O elements uniformly distribute in both catalysts. Besides, a small amount of N element can be detected (atomic ratio 2.75%), originating from annealing in  $\text{NH}_3$  atmosphere under high temperature. Because of its lone pair of electrons, N can affect  $\text{CO}_2$  and intermediates adsorption then boost the  $\text{CO}_2\text{RR}$  conversion performance [39].

The chemical composition, valance states were investigated by X-ray photoelectron spectroscopy (XPS). As exhibited in Fig. 2a, the feature peaks of Cu 2p spectrum for both  $\text{Cu}_2\text{O}$  and N- $\text{Cu}_2\text{O}$  catalysts are located at 932.1 eV and 952.0 eV, being attributed to the Cu 2p<sub>1/2</sub> and Cu 2p<sub>3/2</sub> of  $\text{Cu}^+$ , respectively [40]. The other two relatively weak peaks for  $\text{Cu}_2\text{O}$  at 934.5 eV and 954.5 eV and the corresponding satellite peaks are

coming from  $\text{Cu}^{2+}$  [41]. Totally, the principal composition and valance state are  $\text{Cu}^+$ , and the existence of trace  $\text{Cu}^{2+}$  is probably caused by the  $\text{Cu}_2\text{O}$  being exposed in the atmosphere [42]. In Fig. 2b, the O1s spectrum for  $\text{Cu}_2\text{O}$  can be fitted into two peaks locate at 529.7 eV and 531.3 eV, associated with the surface absorbed oxygen ( $\text{O}_{\text{ads}}$ ) and crystal lattice oxygen species ( $\text{O}_{\text{latt}}$ ), respectively [43]. An obvious shift of banding energy is observed in N- $\text{Cu}_2\text{O}$  catalyst's O1s spectrum, due to the generation of oxygen vacancies ( $\text{O}_v$ ) caused by N doping [20]. Moreover, the peak ratio between  $\text{O}_{\text{latt}}$  and  $\text{O}_{\text{ads}}$  is the measure of the amount of surface  $\text{O}_v$ . For  $\text{Cu}_2\text{O}$  sample, the value of  $\text{O}_{\text{latt}}/\text{O}_{\text{ads}}$  is 55.9%, while it decreases to 34.7% after N-doping, indicating the generation of  $\text{O}_v$ . The result further confirm that N occupied  $\text{O}_v$  in N- $\text{Cu}_2\text{O}$  sample, which may promote the exposure of reductive Cu active sites [44]. The presence of N in N- $\text{Cu}_2\text{O}$  was further validated by the N 1s spectrum as shown in Fig. 2c. The significant peaks at 399.0 eV and 397.4 eV correspond to oxidized nitrogen (Cu-O-N) and Cu-N bond [45–48]. This is consistent with the aforementioned O1s analysis that O is replaced by N element.

Ex-situ electron paramagnetic resonance (EPR) measurement was employed to further verify the existence of  $\text{O}_v$  in N- $\text{Cu}_2\text{O}$  (Fig. 2d). An apparent signal with a g value of 2.003 is detected, further proving the generation of  $\text{O}_v$  [49,50]. Brunauer-Emmett-Teller (BET) adsorption and desorption test was also carried out to evaluate the surface characteristic of the prepared  $\text{Cu}_2\text{O}$  and N- $\text{Cu}_2\text{O}$  catalysts. As the results shown in Fig. S3, the BET surface area of N- $\text{Cu}_2\text{O}$  is  $8.06 \text{ m}^2 \text{ g}^{-1}$ , which is almost two-fold as that of  $\text{Cu}_2\text{O}$  ( $4.74 \text{ m}^2 \text{ g}^{-1}$ ). The enlarged surface area of N- $\text{Cu}_2\text{O}$  is in favor of increasing the  $\text{CO}_2$  adsorption capacity and active sites of catalyst during the process of electrochemical reduction, which can be proved by the result in Figs. S4 and S5. It can be observed from Fig. S4, the largest adsorbed  $\text{CO}_2$  amount of N- $\text{Cu}_2\text{O}$  is nearly two times as that of  $\text{Cu}_2\text{O}$ , indicating the higher  $\text{CO}_2$  adsorption capability on N- $\text{Cu}_2\text{O}$  catalyst. And the ECSA result in Fig. S5 for the catalysts shows that the active surface area of N- $\text{Cu}_2\text{O}$  catalyst is also larger than that of  $\text{Cu}_2\text{O}$  catalyst. The enlarged active surface area facilitates  $\text{CO}_2\text{RR}$  [51, 52].

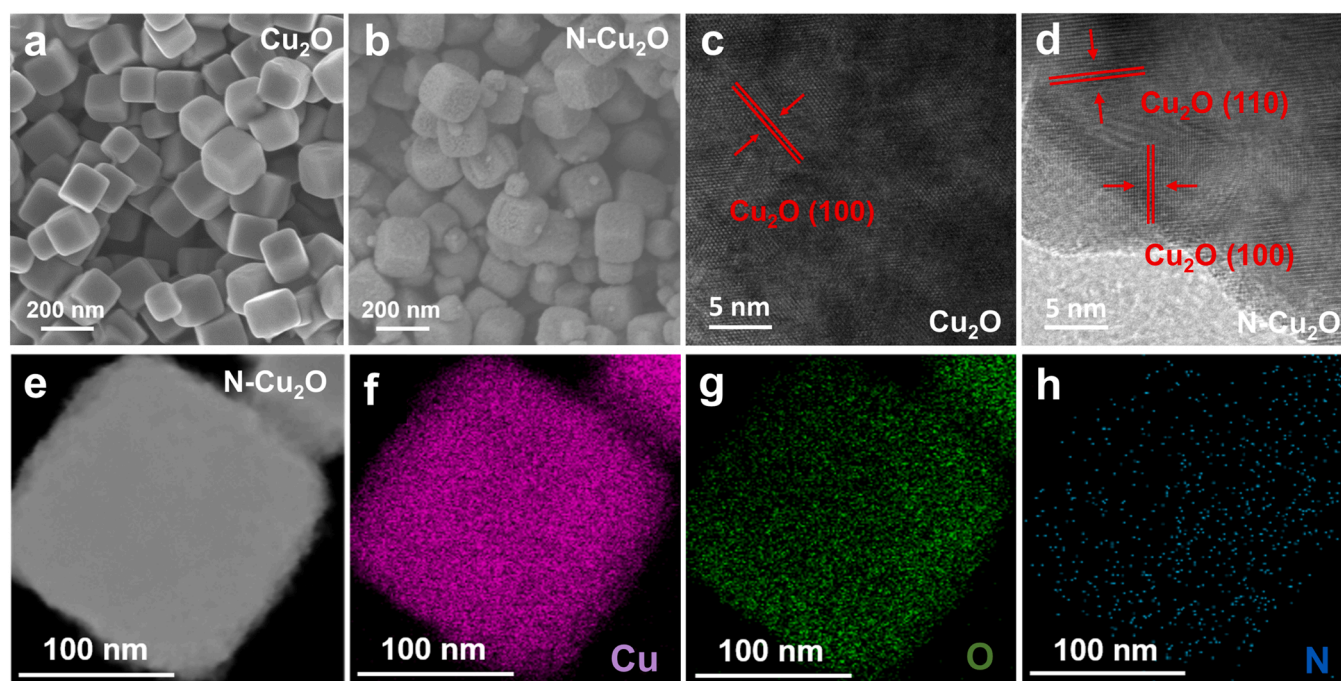


Fig. 1. SEM images of the as-prepared a)  $\text{Cu}_2\text{O}$  and b) N- $\text{Cu}_2\text{O}$  catalysts. HRTEM images and SAED patterns of c)  $\text{Cu}_2\text{O}$  and d) N- $\text{Cu}_2\text{O}$ . EDX mapping images of f) Cu, g) O, and h) N elements in single N- $\text{Cu}_2\text{O}$  particle as shown in e).

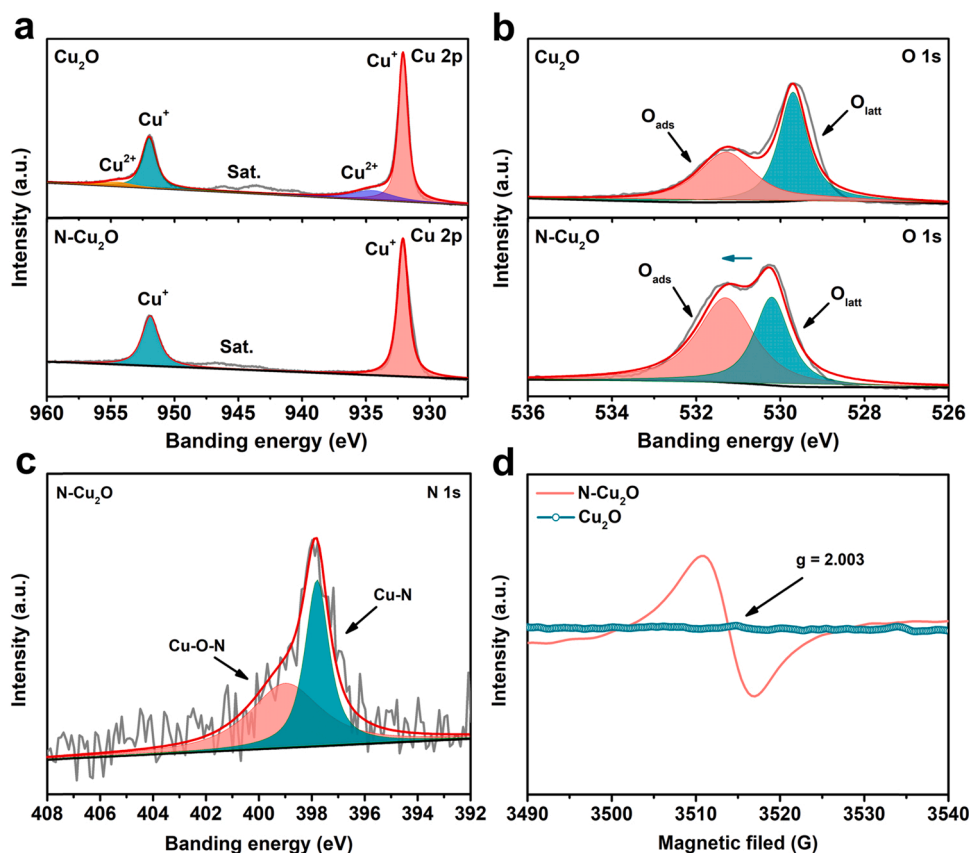


Fig. 2. XPS spectrum of a)  $\text{Cu } 2p$  and b)  $\text{O } 1s$  for  $\text{Cu}_2\text{O}$  and  $\text{N-Cu}_2\text{O}$  catalysts. c)  $\text{N } 1s$  spectrum of  $\text{N-Cu}_2\text{O}$  catalyst. d) EPR spectrum of  $\text{Cu}_2\text{O}$  and  $\text{N-Cu}_2\text{O}$  catalysts.

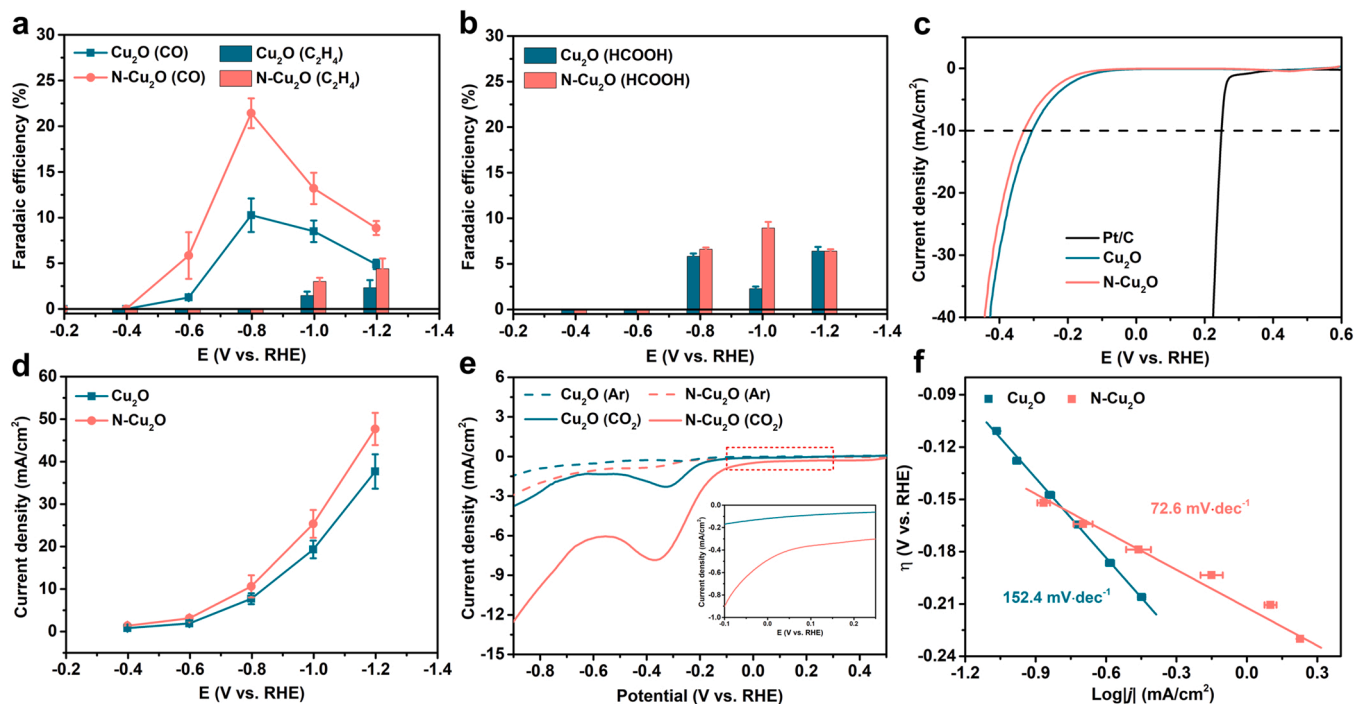


Fig. 3. Faradaic efficiency of a)  $\text{CO}$  and  $\text{C}_2\text{H}_4$  and b)  $\text{HCOOH}$  on  $\text{Cu}_2\text{O}$  and  $\text{N-Cu}_2\text{O}$  catalysts at different potentials. c) HER performance of  $\text{Pt/C}$ ,  $\text{Cu}_2\text{O}$  and  $\text{N-Cu}_2\text{O}$  in 0.5 M  $\text{H}_2\text{SO}_4$ . d) Current density of  $\text{CO}_2$  electroreduction at each applied potential, e) LSV curves in the range of 0.5 V to -0.9 V and f) Tafel plots of  $\text{Cu}_2\text{O}$  and  $\text{N-Cu}_2\text{O}$  catalysts.

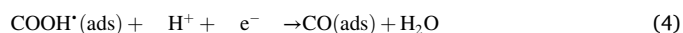
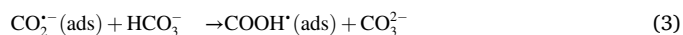


### 3.2. Electrochemical behaviors of catalysts

CO<sub>2</sub> electroreduction behavior of the Cu<sub>2</sub>O and N-Cu<sub>2</sub>O electrocatalysts was evaluated by chronoamperometric electrolysis under constant potential. The working potential ranges from −0.4 to −1.2 V (vs. RHE) at an interval of 0.2 V. The Faradic efficiency (FE) of CO production for N-Cu<sub>2</sub>O is higher than that of Cu<sub>2</sub>O at all the applied potentials, as shown in Fig. 3a. The higher Faradic efficiency of CO at −0.8 V for N-Cu<sub>2</sub>O is one-fold elevated as compared to the Cu<sub>2</sub>O under identical conditions. Besides, the C<sub>2</sub>H<sub>4</sub> production is also two times as high as that of Cu<sub>2</sub>O at −1.2 V, demonstrating the excellent CO<sub>2</sub>RR performance of N-Cu<sub>2</sub>O towards the production of C<sub>2</sub> chemicals. Additionally, a small amount (faradic efficiency 2–9%) of liquid product (HCOOH) is found during the CO<sub>2</sub>RR on both catalysts (Fig. 3b). And the long-term stability test was then proceeded in CO<sub>2</sub> saturated 0.5 M KHCO<sub>3</sub> electrolyte under −0.8 V (vs. RHE) for 5400 s. In the long-term experiment, the current density remains stable and the faradic efficiencies for CO and HCOOH production are always higher than 20% and 5% using the N-Cu<sub>2</sub>O catalyst, respectively (Fig. S6). That indicates the high stability of the catalysts during the long-time reaction. Hydrogen evolution reaction (HER) test was further operated to evaluate the H<sub>2</sub> generation performance of Cu<sub>2</sub>O and N-Cu<sub>2</sub>O in Fig. 3c, it is found that HER is suppressed after N doping on the Cu<sub>2</sub>O. This is consistent with the result that CO<sub>2</sub>RR for N-Cu<sub>2</sub>O is superior than Cu<sub>2</sub>O catalyst at this condition. The current density of Cu<sub>2</sub>O and N-Cu<sub>2</sub>O during the CO<sub>2</sub> electroreduction procedure is displayed in Fig. 3d. As evidence of the figure, the current density of N-Cu<sub>2</sub>O is much higher than that of Cu<sub>2</sub>O at the applied potentials. The current density disparity increases when the applied potential shifts to more negative stages, indicating a faster electron transfer rate of N-Cu<sub>2</sub>O. The electroanalytical behavior of those two catalysts was simultaneously operated in both Ar and CO<sub>2</sub>-saturated 0.5 M KHCO<sub>3</sub> electrolyte by Linear sweep voltammetry (LSV) at the scan rate of 20 mV/s, respectively. As shown in Fig. 3e, no prominent peaks are observed in the Ar saturated electrolytes. In contrast, the large cathodic peaks are observed in the CO<sub>2</sub>-saturated KHCO<sub>3</sub> solution between −0.35 V and −0.45 V, which can be ascribed to the electrochemical reaction between oxide species and CO<sub>2</sub> [39]. Notably, N-Cu<sub>2</sub>O exhibits an earlier onset potential and a higher current density than Cu<sub>2</sub>O. At larger overpotentials, the N-Cu<sub>2</sub>O catalyst shows a better CO<sub>2</sub>RR activity than Cu<sub>2</sub>O. Based on the electrochemical results, the N-doping could significantly enhance the electrochemical CO<sub>2</sub> reduction performance of Cu<sub>2</sub>O. The charge transfer resistance of the catalysts was performed by Electrochemical impedance spectroscopy (EIS) test under −0.6 V (vs. RHE) over a frequency range from 10 to 10<sup>5</sup> Hz. The Nyquist plots of N-Cu<sub>2</sub>O catalyst in Fig S7 possess a smaller semicircle than Cu<sub>2</sub>O in the high-frequency region. This indicates small internal solution resistance and faster charge transfer-rate of N-Cu<sub>2</sub>O in the system [52]. To in depth understand the improved CO<sub>2</sub>RR performance of N-Cu<sub>2</sub>O, the reaction kinetic analysis, real-time spectrum measurement, and theoretical calculations were carried out in succession.

It is widely accepted that the selectivity is highly dependent on the competitive adsorption of intermediates (like CO<sub>2</sub><sup>•−</sup> and COOH<sup>•</sup> etc.) and the reaction kinetic energy barrier, which involves the RDS for electrochemical reduction of CO<sub>2</sub> [53]. Hence, Tafel plot was tested as shown in Fig. 3f. Tafel slope of Cu<sub>2</sub>O is 152.4 mV dec<sup>−1</sup>, which approaches the theoretical value (118 mV dec<sup>−1</sup>), indicating that the first one-electron transfer step to form the adsorbed CO<sub>2</sub><sup>•−</sup> intermediate (Eq. 2) is RDS [54–57]. Notably, a Tafel slope of 72.6 mV dec<sup>−1</sup> is obtained at N-Cu<sub>2</sub>O, which is close to the theoretical value (59 mV dec<sup>−1</sup>), indicating a rapid one-electron transfer step followed by a protonation step of CO<sub>2</sub><sup>•−</sup> (RDS step) to form COOH<sup>•</sup> intermediate (Eq. 3). Therefore, the Eq. (2) is not RDS step for N-Cu<sub>2</sub>O [54,55,58]. The high kinetic activity and significantly reduced Tafel slope clearly confirms the efficiency of N-doping in enhancing the CO<sub>2</sub>RR activity on Cu<sub>2</sub>O. Based on the experimental results, the Faradaic efficiency of CO is much larger than HCOOH, demonstrating that after forming the adsorbed COOH<sup>•</sup>

intermediates, the reaction of CO<sub>2</sub> tends to choose the way of producing CO (Eq. 4). It is also further proved by the in-situ Raman spectrum. The reaction procedures are shown as follows:



### 3.3. In-situ Raman spectrum analysis

To gain a visualized insight into the CO<sub>2</sub>RR enhancement on N-Cu<sub>2</sub>O, the reaction intermediates during CO<sub>2</sub>RR were monitored in real-time by in-situ SERS measurement in CO<sub>2</sub>-purged 0.5 M KHCO<sub>3</sub> solution at different potentials from 0.4 V to −0.8 V (vs. RHE). Raman spectrum was collected at an interval of 0.1 V. Under open current potential (OCP) in Fig. S8, four bands centered at 220, 429, 520 and 621 cm<sup>−1</sup> are detected in the orange and blue line, belonging to the typical Raman shift of Cu<sub>2</sub>O [59,60]. Besides, the peak at 1017 cm<sup>−1</sup> is attributed to ν HCO<sub>3</sub><sup>−</sup> of adsorbed electrolyte (KHCO<sub>3</sub>). As observed from Fig. 4a and c, under the initial potentials, the peaks at 1366 cm<sup>−1</sup> and 1659 cm<sup>−1</sup> are ascribed to disordered carbon and graphite carbon of carbon paper, respectively [61]. When the applied potentials shift negatively, new peaks appear for both Cu<sub>2</sub>O and N-Cu<sub>2</sub>O. Notably, the typical Cu<sub>2</sub>O peaks disappear due to the immediately partial reduction of Cu<sub>2</sub>O surface species to metallic Cu [42]. These new peaks of N-Cu<sub>2</sub>O catalyst are observed earlier than that of Cu<sub>2</sub>O at the more positive applied potential. The intensities from N-Cu<sub>2</sub>O are much more intensive as reference to the Cu<sub>2</sub>O. After N doping, the intensity of characteristic peaks increases, which is beneficial for detecting the intermediates during CO<sub>2</sub>RR by in-situ SERS and boosting C<sub>2</sub> production. As clearly shown in Fig. 4b and d, the peak intensity is significantly increased after N doping. The highest intensity for N-Cu<sub>2</sub>O is about 6400 a.u., in good contrast of only 750 a.u. for Cu<sub>2</sub>O, suggesting that the N doping can evidently enhance the binding strength of intermediates for CO<sub>2</sub>RR and improve the C<sub>2</sub>H<sub>4</sub> Faradic efficiency, as mentioned in Fig. 3a.

When the applied potential shifts to 0.2 V for N-Cu<sub>2</sub>O, as shown in part B of Fig. 4c, new peaks appear at 1067 cm<sup>−1</sup> and 1548 cm<sup>−1</sup>. The peak at 1067 cm<sup>−1</sup> corresponds to the stretching vibration of chemisorbed carbonate (ν CO<sub>3</sub><sup>2−</sup> mode), arising from the deprotonation of KHCO<sub>3</sub> electrolyte. The peak at 1548 cm<sup>−1</sup> (blue region) can be assigned to asymmetric stretching of OC\*O<sup>•</sup>, marked as ν<sub>as</sub> CO<sub>2</sub><sup>•−</sup>, which is well-accepted as the starting adsorption mode of intermediate for HCOOH production [62]. On the other hand, the appearance of 1067 cm<sup>−1</sup> peak is noticed at a more negative bias (0 V) for Cu<sub>2</sub>O catalyst (part B of Fig. 4a), similar to the peak of ν<sub>as</sub> CO<sub>2</sub><sup>•−</sup> (−0.1 V), indicating the CO<sub>2</sub><sup>•−</sup> intermediate adsorption on Cu<sub>2</sub>O is more difficult than that on N-Cu<sub>2</sub>O. Therefore, Eq. (2) is the RDS for Cu<sub>2</sub>O. In addition, the introduction of N promotes the reaction from Eqs. (2) to (3), making it easier for forming COOH<sup>•</sup> intermediate.

Notably, the peak locating at 1366 cm<sup>−1</sup> (red region) in part B of both Fig. 4a and c is the vibration peak of symmetrical stretching \*COOH, which is overlapped with the peak of disordered carbon, further proved by the Raman in Fig. S9 [20]. The intensity of the disordered carbon peak remains unchanged on pure carbon paper at all the applied potentials [20,61]. Besides, no other peaks appear, indicating that the carbon paper only functions as a current collector during the whole process of CO<sub>2</sub>RR. When the N-Cu<sub>2</sub>O catalyst is loaded on the carbon paper, with the applied potential shifts more negative, the intensity of the 1366 cm<sup>−1</sup> peak increases at 0.2 V, then decreases gradually during the reaction process in Fig. 4c. As a result, the increase of the peak intensity at 1366 cm<sup>−1</sup> actually originates from \*COOH vibration, an important intermediate for the production of CO according to the

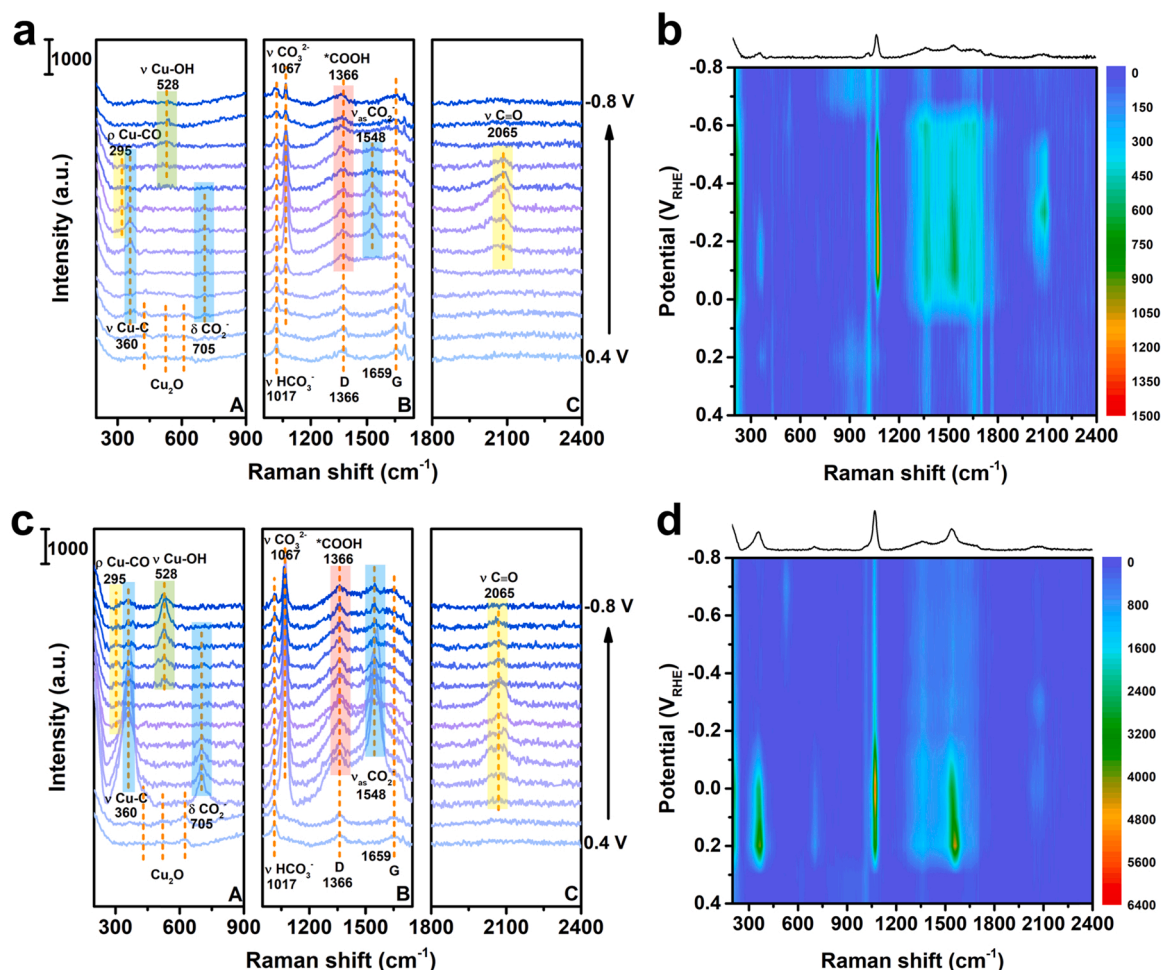


**Fig. 4.** a) In-situ Raman spectrum and b) Hot spot diagram of Cu<sub>2</sub>O under the potentials range from 0.4 V to -0.8 V (vs RHE) at an interval of 0.1 V. c) In-situ Raman spectrum and d) Hot spot diagram of N-Cu<sub>2</sub>O under the potentials range from 0.4 V to -0.8 V (vs RHE) at an interval of 0.1 V.

reported literature [63]. This indicates that \*COOH is formed earlier on N-Cu<sub>2</sub>O. The faster decrease of this peak should be ascribed to the reaction of Eq. (4), where the \*COOH transforms to \*CO intermediate.

Interestingly, the signal at 360 cm<sup>-1</sup> (blue region), shown in part A of Fig. 4c, exhibits a similar trend to that of ν<sub>as</sub> CO<sub>2</sub><sup>-</sup>. When the applied potentials shift from 0.2 to -0.8 V, the intensity of 1548 cm<sup>-1</sup> and 360 cm<sup>-1</sup> decreases gradually for N-Cu<sub>2</sub>O, which proves that both peaks are associated with the same species. As reported, the 360 cm<sup>-1</sup> peak is from the vibration of Cu-C bonding in the OC\*O\* intermediate, where carbon atom is coordinated with Cu surface [62]. Obviously, the peaks of ν<sub>as</sub> CO<sub>2</sub><sup>-</sup> and ν Cu-C existed from 0.2 V to -0.8 V during the CO<sub>2</sub>RR for the N-Cu<sub>2</sub>O catalyst. While using Cu<sub>2</sub>O catalyst, those two peaks are observed in the small applied potential range during the electrochemical reaction. Due to the weak adsorption strength, the peak locating at 705 cm<sup>-1</sup> (blue region) can only be detected in a relatively small range for both catalysts in part A of Fig. 4c, which is in-plane CO<sub>2</sub><sup>-</sup> mode of OC\*O\*, marked as δ CO<sub>2</sub><sup>-</sup> (shown in Fig. S10) [62].

Furthermore, the introduction of N also promotes the dissociation of COOH during the CO<sub>2</sub> reduction (Eq. 4). In part C of Fig. 4a and c, a peak located at 2065 cm<sup>-1</sup> (yellow region) can be assigned to the C=O stretching vibration [64]. This peak could be reductively dissociated from \*COOH, and is the most common adsorption mode of \*CO on Cu catalysts, leading to the production of CO and C<sub>2</sub>H<sub>4</sub> on Cu. When the applied potential reaches -0.3 V, the \*CO peak intensity is much stronger, as shown in Fig. 4b and d, indicating the most abundant \*CO intermediates are adsorbed on the surface of the electrode at this state, thus facilitating sequential reduction of \*CO and C-C coupling of

neighbor \*CO. Correspondingly, adsorbed Cu-CO (peak locates at 295 cm<sup>-1</sup>, yellow region), a comparatively weak adsorption mode can be detected during CO<sub>2</sub>RR for N-Cu<sub>2</sub>O catalyst [65]. These results unambiguously prove that N doping could efficiently enhance the adsorption of intermediates during CO<sub>2</sub> electroreduction on Cu<sub>2</sub>O.

In order to further investigate the evolution of reaction intermediates during CO<sub>2</sub>RR, the long-term CO<sub>2</sub>RR was performed under the constant potential of -0.3 V for the N-Cu<sub>2</sub>O catalyst, as presented in Fig. 5. The intensity and volume of peak \*CO (2065 cm<sup>-1</sup>, yellow region) are nearly unchanged with increasing reaction time. Besides, no other peaks appear around the \*CO peak. Until the reaction time reaches 900 s, a

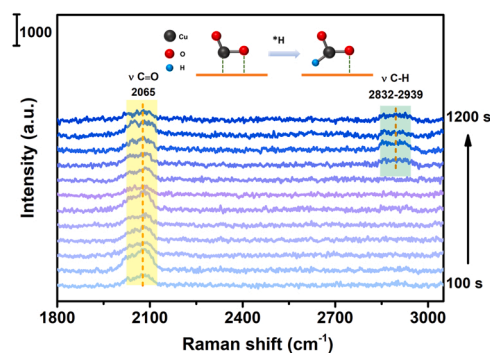


**Fig. 5.** In-situ Raman spectrum for N-Cu<sub>2</sub>O catalyst under long-time electroreduction.

new broad peak is found at the range of 2832–2939  $\text{cm}^{-1}$  (green region), which can be assigned to the C-H stretching vibration ( $\nu$  C-H) of the  $\text{HCOO}^*$  intermediate, its corresponding product  $\text{HCOOH}$  is detected after  $\text{CO}_2\text{RR}$  reaction by HNMR. This agrees well with the multiple binding configurations of N-Cu<sub>2</sub>O catalysis [62].

The area ratio of  $\nu \text{CO}_3^{2-}$  to  $\nu \text{HCO}_3^-$  peaks in the Raman spectra is used to evaluate the surface pH of catalysts [65]. As is shown in Fig. S11, it is observed that the peak area ratio of  $\nu \text{CO}_3^{2-}$  ( $1067 \text{ cm}^{-1}$ )/ $\nu \text{HCO}_3^-$  ( $1017 \text{ cm}^{-1}$ ) on the N-Cu<sub>2</sub>O is larger than that of Cu<sub>2</sub>O, indicating a higher pH value of N-Cu<sub>2</sub>O during  $\text{CO}_2\text{RR}$ . According to reports, higher pH is favorable for  $\text{C}_2^+$  production [62,66]. The higher pH value of N-Cu<sub>2</sub>O indeed promotes the  $\text{C}_2\text{H}_4$  production and achieve the higher faradic efficiency than Cu<sub>2</sub>O in this work. Meanwhile, the applied potential ranges between  $-0.4 \text{ V}$  and  $-0.8 \text{ V}$ , a new peak appears at  $528 \text{ cm}^{-1}$  (green region), as shown in Fig. 4c, which can be assigned to  $\nu$  Cu-OH, resulting from the increasing pH value with reduction [53]. The improved activity of  $\text{CO}_2\text{RR}$  by N doping will be further verified by theoretical calculation.

### 3.4. Theoretical investigation

DFT calculation was conducted by VASP. The adsorption energy ( $E$ ) of  $\text{CO}_2$  on the substrate is calculated according to the following reaction:

$$E_{\text{ad}} = E_{\text{tot}} - E_{\text{substrate}} - E_{\text{CO}_2} \quad (5)$$

where  $E_{\text{ad}}$  is the adsorption energy,  $E_{\text{tot}}$  is the total energy of the molecule on the substrate,  $E_{\text{substrate}}$  is the energy of the substrate,  $E_{\text{CO}_2}$  is the energy of the  $\text{CO}_2$  adsorbed.

The adsorption and activation of  $\text{CO}_2$  are the key steps during the process of  $\text{CO}_2\text{RR}$  [67]. The calculated adsorption energy for  $\text{CO}_2$  molecules on pure Cu<sub>2</sub>O is about  $-0.068 \text{ eV}$ , while that on N-Cu<sub>2</sub>O is  $-2.83 \text{ eV}$ . These negative values indicate that both Cu<sub>2</sub>O and N-Cu<sub>2</sub>O are favorable for the adsorption of  $\text{CO}_2$ . The higher value for N-Cu<sub>2</sub>O suggests the adsorption of  $\text{CO}_2$  is more thermodynamically favorable, and the introduction of N is beneficial for the adsorption of  $\text{CO}_2$  on the surface of the catalysts.

Besides, after optimization, the average length of the C=O bond in the  $\text{CO}_2$  molecule ( $1.16 \text{ \AA}$ ) is only slightly elongated on the Cu<sub>2</sub>O surface ( $1.18 \text{ \AA}$ ), and the  $\text{CO}_2$  molecule is still in a linear model with an angle of  $180^\circ$  (Fig. 6a). However, on the surface of N-Cu<sub>2</sub>O, it is evident that the C atom from the  $\text{CO}_2$  molecule is attracted by the N atom from

the substrate, indicating a strong interaction between the N and C atoms. Also, one O atom from the  $\text{CO}_2$  molecule is adsorbed by the Cu atom from the substrate. These two bonds make the  $\text{CO}_2$  molecule adsorbed on the substrate. As a result, the average length of the C=O bond in the  $\text{CO}_2$  molecules increases to  $1.24 \text{ \AA}$  and  $1.30 \text{ \AA}$ , and the  $\text{CO}_2$  molecule is bent with the angle of  $127.8^\circ$  (Fig. 6b). These results strongly indicate that the  $\text{CO}_2$  molecule can be easily activated on the N-Cu<sub>2</sub>O.

The charge distribution map of N-Cu<sub>2</sub>O- $\text{CO}_2$  is shown in Fig. 6c, where the yellow region corresponds to the electrons. It can be found that the electron mainly distributes on the oxygen atoms, suggesting the transfer of electron from Cu to the O. This is consistent with the ionic bonding of Cu<sub>2</sub>O. The introduction of N also gains some electrons. In the bader analysis (Table 1), it can also be found that the value of N atom is 6.15, which is higher than that of its isolated state.

The reduction of  $\text{CO}_2$  involves two important intermediates of  $^*\text{COOH}$  and  $^*\text{CO}$  as evidenced by the Raman spectroscopy. Therefore, the energy of these two intermediates on Cu<sub>2</sub>O and N-Cu<sub>2</sub>O is investigated. As shown in Fig S12, the first step for the formation of  $^*\text{COOH}$  is  $-4.72 \text{ eV}$ , lower than the previous step, suggesting the formation of  $^*\text{COOH}$  is favorable. Besides, it is lower than the value of Cu<sub>2</sub>O ( $-3.01 \text{ eV}$ ), indicating that the presence of N is beneficial to the formation of  $^*\text{COOH}$ . Subsequently, the formation of  $^*\text{CO}$  needs to overcome an energy barrier. In this step, the barrier on N-Cu<sub>2</sub>O ( $-2.56$  to  $-4.72 = 2.16 \text{ eV}$ ) is smaller than that on Cu<sub>2</sub>O ( $-0.05$  to  $-3.01 = 2.96 \text{ eV}$ ), this also confirms the benefit of introducing N element.  $^*\text{CO}$  is an important intermediate to form CO and  $\text{C}_2\text{H}_4$ . Based on the DFT calculation, the adsorption energy of  $^*\text{CO}$  is evaluated. The desorption energy of  $^*\text{CO}$  to form CO on Cu<sub>2</sub>O is  $0.05 \text{ eV}$ , and it is  $2.95 \text{ eV}$  on N-Cu<sub>2</sub>O, demonstrating the larger adsorption energy of  $^*\text{CO}$

**Table 1**

Number of valence electrons for Cu, O and N elements on  $\text{CO}_2$  adsorbed Cu<sub>2</sub>O and N-Cu<sub>2</sub>O.

Element	Isolated state	Average value of state in Cu <sub>2</sub> O	Average value of state in N-doped Cu <sub>2</sub> O
Cu in the substrate	11	10.45	10.44
O in the substrate	6	7.09	7.09
N in the substrate	5	–	6.15

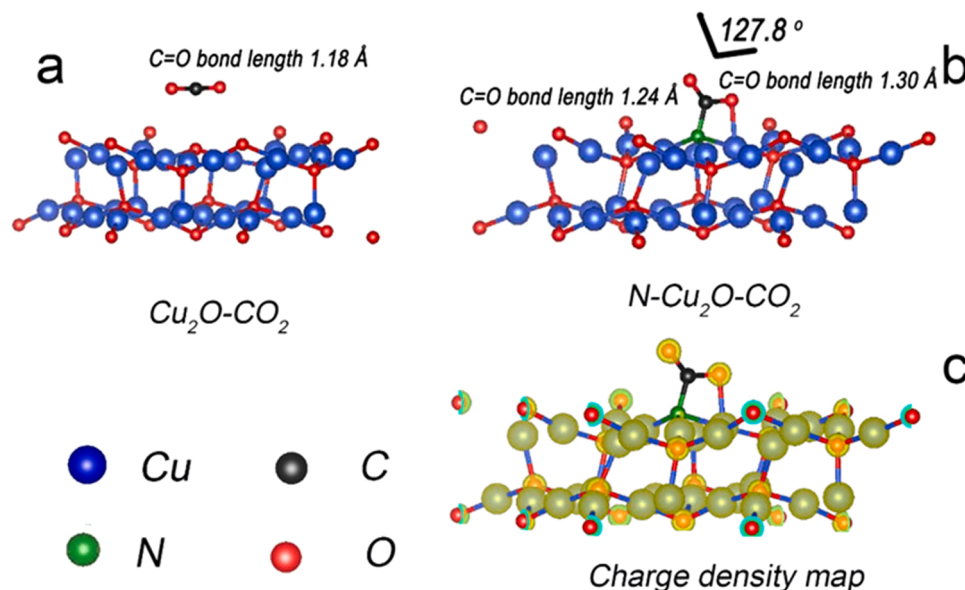


**Fig. 6.** Structure of a) Cu<sub>2</sub>O- $\text{CO}_2$ , b) N-Cu<sub>2</sub>O- $\text{CO}_2$  and c) charge density map of N-Cu<sub>2</sub>O- $\text{CO}_2$ .



on N-Cu<sub>2</sub>O. Hence, the \*CO is stabilized on N-Cu<sub>2</sub>O, this result is consistent with the in-situ Raman result that N doping could enhance the binding strength of intermediates.

#### 4. Conclusions

Reaction intermediates on N-Cu<sub>2</sub>O catalyst are detected, and the optimized reaction procedure for CO<sub>2</sub>RR has been profoundly analyzed. Based on the results of in-situ surface enhanced Raman and theoretical calculations for both pristine Cu<sub>2</sub>O and N-Cu<sub>2</sub>O catalysts, it is unveiled that N doping can efficiently improve the CO<sub>2</sub> adsorption capacity and enhance the binding strength of critical intermediates during CO<sub>2</sub>RR, especially for OC\*O\*, \*COOH and \*CO, favorably contributing to the production of CO and C<sub>2</sub>H<sub>4</sub>. According to Tafel plots, N doping transformed the traditional RDS step to CO<sub>2</sub><sup>•-</sup> + HCO<sub>3</sub><sup>-</sup> → COOH<sup>•</sup> + CO<sub>3</sub><sup>2-</sup>. Moreover, the proceeding step of COOH<sup>•</sup> (ads) + H<sup>+</sup> + e<sup>-</sup> → CO (ads) + H<sub>2</sub>O was considerably fastened, resulting in much enhanced CO<sub>2</sub> reduction kinetics over N-Cu<sub>2</sub>O as compared to the pristine Cu<sub>2</sub>O. This strategy of intermediates stabilization and reaction process optimization by heteroatom doping is facile and significant in better understanding the electrochemical reduction of CO<sub>2</sub>.

#### CRedit authorship contribution statement

**Chunliu Yan:** Sample preparation, Methodology, Investigation, Writing – original draft. **Wen Luo:** Investigation, Data curation. **Huimin Yuan:** Investigation, Data curation. **Guiyu Liu:** Investigation, Data curation. **Rui Hao:** Investigation, Data curation. **Ning Qin:** Investigation, Data curation. **Zhiqiang Wang:** Investigation, Data curation. **Kun Liu:** Investigation, Data curation. **Zhenyu Wang:** Investigation, Data curation. **Duhu Cui:** Conceptualization, Supervision, Writing – review & editing. **Zhuofeng Hu:** Conceptualization, Supervision, Writing – review & editing. **Yangchun Lan:** Conceptualization, Supervision, Writing – review & editing. **Zhouguang Lu:** Conceptualization, Supervision, Writing – review & editing.

#### Declaration of Competing Interest

The authors declare that they have no known competing financial interests or personal relationships that could have appeared to influence the work reported in this paper.

#### Acknowledgements

This work was supported by Shenzhen NSQKJJ under grant funding (K20799112) and by the Basic Research Project of the Science and Technology Innovation Commission of Shenzhen (JCYJ20200109141640095), the National Natural Science Foundation of China (21875097), the Leading Talents of Guangdong Province Program (2016LJ06C536), Shenzhen Key Laboratory of Interfacial Science and Engineering of Materials (ZDSYS20200421111401738), Guangdong-Hong Kong-Macao Joint Laboratory (2019B121205001). This work was also supported by the National Natural Science Foundation of China (Grant No. 51902357), the Natural Science Foundation of Guangdong Province, China (2019A1515012143), the Start-up Funds for High-Level Talents of Sun Yat-sen University (38000-18841209) and the Fundamental Research Funds for the Central Universities (38000-31610622). The theoretical calculation is supported by National Supercomputer Center in Guangzhou, National Supercomputing Center in Shenzhen (Shenzhen Cloud Computing Center), and Center for Computational Science and Engineering at SUSTech.

#### Appendix A. Supporting information

Supplementary data associated with this article can be found in the online version at [doi:10.1016/j.apcatb.2022.121191](https://doi.org/10.1016/j.apcatb.2022.121191).

#### References

- [1] D. Gao, R.M. Arán-Ais, H.S. Jeon, B. Roldan Cuenya, Rational catalyst and electrolyte design for CO<sub>2</sub> electroreduction towards multicarbon products, *Nat. Catal.* 2 (2019) 198–210.
- [2] X. Ma, J. Du, H. Sun, F. Ye, X. Wang, P. Xu, C. Hu, Li Zhang, a, D. Liu, Boron, nitrogen co-doped carbon with abundant mesopores for efficient CO<sub>2</sub> electroreduction, *Appl. Catal. B: Environ.* 298 (2021), 120543.
- [3] X. Chena, D. Ma, Bo Chen, K. Zhang, Ru Zou, X. Wu, Q. Zhu, Metal-organic framework derived mesoporous carbon nanoframes embedded with atomically dispersed Fe-Nx active sites for efficient bifunctional oxygen and carbon dioxide electroreduction, *Appl. Catal. B: Environ.* 267 (2020), 118720.
- [4] M.B. Ross, P. De Luna, Y. Li, C.-T. Dinh, D. Kim, P. Yang, E.H. Sargent, Designing materials for electrochemical carbon dioxide recycling, *Nat. Catal.* 2 (2019) 648–658.
- [5] H. Liu, Y. Zhu, J. Ma, Z. Zhang, W. Hu, Atomically thin catalysts: recent advances in atomic-level engineering of nanostructured catalysts for electrochemical CO<sub>2</sub> reduction, *Adv. Funct. Mater.* 30 (2020), 2070107.
- [6] T. Zheng, K. Jiang, H. Wang, Recent advances in electrochemical CO<sub>2</sub>-to-CO conversion on heterogeneous catalysts, *Adv. Mater.* 30 (2018), 1802066.
- [7] N. Han, P. Ding, L. He, Y. Li, Y. Li, Promises of main group metal-based nanostructured materials for electrochemical CO<sub>2</sub> reduction to formate, *Adv. Energy Mater.* 10 (2020), 1902338.
- [8] L. Wang, W. Chen, D. Zhang, Y. Du, R. Amal, S. Qiao, J. Wu, Z. Yin, Surface strategies for catalytic CO<sub>2</sub> reduction: from two-dimensional materials to nanoclusters to single atoms, *Chem. Soc. Rev.* 48 (2019) 5310–5349.
- [9] D.-H. Nam, P. De Luna, A. Rosas-Hernández, A. Thevenon, F. Li, T. Agapie, J. C. Peters, O. Shekiah, M. Eddaoudi, E.H. Sargent, Molecular enhancement of heterogeneous CO<sub>2</sub> reduction, *Nat. Mater.* 19 (2020) 266–276.
- [10] L. Lv, X. He, J. Wang, Y. Ruan, S. Ouyang, H. Yuan, T. Zhang, Charge localization to optimize reactant adsorption on KCu<sub>2</sub>S<sub>4</sub>/CuO interfacial structure toward selective CO<sub>2</sub> electroreduction, *Appl. Catal. B: Environ.* 298 (2021), 120531.
- [11] J. Huang, M. Mensi, E. Oveisi, V. Mantella, R. Buonsanti, Structural sensitivities in bimetallic catalysts for electrochemical CO<sub>2</sub> reduction revealed by Ag-Cu nanodimers, *J. Am. Chem. Soc.* 141 (2019) 2490–2499.
- [12] W. Luc, B.H. Ko, S. Kattel, S. Li, D. Su, J.G. Chen, F. Jiao, SO<sub>2</sub>-induced selectivity change in CO<sub>2</sub> electroreduction, *J. Am. Chem. Soc.* 141 (2019) 9902–9909.
- [13] Y. Zhao, X. Liu, D. Chen, Z. Liu, Q. Yang, X. Lin, M. Peng, P. Liu, Y. Tan, Atomic-level-designed copper atoms on hierarchically porous gold architectures for high-efficiency electrochemical CO<sub>2</sub> reduction, *Sci. China Mater.* 64 (2021) 1900–1909.
- [14] J. Pan, Y. Sun, P. Deng, F. Yang, S. Chen, Q. Zhou, Ho Parkb, H. Liu, B. Xia, Hierarchical and ultrathin copper nanosheets synthesized via galvanic replacement for selective electrocatalytic carbon dioxide conversion to carbon monoxide, *Appl. Catal. B: Environ.* 255 (2019), 117736.
- [15] A.N. Grace, S.Y. Choi, M. Vinoba, M. Bhagiyalakshmi, D.H. Chu, Y. Yoon, S. C. Nam, S.K. Jeong, Electrochemical reduction of carbon dioxide at low overpotential on a polyaniline/Cu<sub>2</sub>O nanocomposite based electrode, *Appl. Energy* 120 (2014) 85–94.
- [16] F. Franco, C. Rettenmaier, H.S. Jeon, B. Roldan Cuenya, Transition metal-based catalysts for the electrochemical CO<sub>2</sub> reduction: from atoms and molecules to nanostructured materials, *Chem. Soc. Rev.* 49 (2020) 6884–6946.
- [17] S.Y. Lee, H. Jung, N.-K. Kim, H.-S. Oh, B.K. Min, Y.J. Hwang, Mixed copper states in anodized Cu electrocatalyst for stable and selective ethylene production from CO<sub>2</sub> reduction, *J. Am. Chem. Soc.* 140 (2018) 8681–8689.
- [18] S. Popović, M. Smiljanić, P. Jovanović, J. Vavra, R. Buonsanti, N. Hodnik, Stability and degradation mechanisms of copper-based catalysts for electrochemical CO<sub>2</sub> reduction, *Angew. Chem. Int. Ed.* 59 (2020) 14736–14746.
- [19] T.-T. Zhuang, Z.-Q. Liang, A. Seifitokaldani, Y. Li, P. De Luna, T. Burdyny, F. Che, F. Meng, Y. Min, R. Quintero-Bermudez, C.T. Dinh, Y. Pang, M. Zhong, B. Zhang, J. Li, P.-N. Chen, X.-L. Zheng, H. Liang, W.-N. Ge, B.-J. Ye, D. Sinton, S.-H. Yu, E. H. Sargent, Steering post C-C coupling selectivity enables high efficiency electroreduction of carbon dioxide to multi-carbon alcohols, *Nat. Catal.* 1 (2018) 421–428.
- [20] Q. Wan, J. Zhang, B. Zhang, D. Tan, L. Yao, L. Zheng, F. Zhang, L. Liu, X. Cheng, B. Han, Boron-doped CuO nanobundles for electroreduction of carbon dioxide to ethylene, *Green Chem.* 22 (2020) 2750–2754.
- [21] C. Ma, P. Hou, X. Wang, Z. Wang, W. Lia, P. Kang, Carbon nanotubes with rich pyridinic nitrogen for gas phase CO<sub>2</sub> electroreduction, *Appl. Catal. B: Environ.* 250 (2019) 347–354.
- [22] F. Ni, H. Yang, Y. Wen, H. Bai, L. Zhang, C. Cui, S. Li, S. He, T. Cheng, B. Zhang, H. Peng, N-modulated Cu<sup>+</sup> for efficient electrochemical carbon monoxide reduction to acetate, *Sci. China Mater.* 63 (2020) 2606–2612.
- [23] J.-C. Lee, J.-Y. Kim, W.-H. Joo, D. Hong, S.-H. Oh, B. Kim, G.-D. Lee, M. Kim, J. Oh, Y.-C. Joo, Thermodynamically driven self-formation of copper-embedded nitrogen-doped carbon nanofiber catalysts for a cascade electroreduction of carbon dioxide to ethylene, *J. Mater. Chem. A* 8 (2020) 11632–11641.
- [24] M. Kuang, A. Guan, Z. Gu, P. Han, L. Qian, G. Zheng, Enhanced N-doping in mesoporous carbon for efficient electrocatalytic CO<sub>2</sub> conversion, *Nano Res.* 12 (2019) 2324–2329.
- [25] D. Tan, C. Cui, J. Shi, Z. Luo, B. Zhang, X. Tan, B. Han, L. Zheng, J. Zhang, J. Zhang, Nitrogen-carbon layer coated nickel nanoparticles for efficient electrocatalytic reduction of carbon dioxide, *Nano Res.* 12 (2019) 1167–1172.
- [26] Y.F. Wang, Y.X. Li, Z.Y. Wang, P. Allan, F.C. Zhang, Z.G. Lu, Reticular chemistry in electrochemical carbon dioxide reduction, *Sci. China Mater.* 63 (2020) 1113–1141.
- [27] X. Li, S. Wang, L. Li, Y. Sun, Y. Xie, Progress and perspective for in situ studies of CO<sub>2</sub> reduction, *J. Am. Chem. Soc.* 142 (2020) 9567–9581.



- [28] S.S. Wu, Y.G. Zhu, Y.F. Huo, Y.C. Luo, L.H. Zhang, Y. Wan, B. Nan, L.J. Cao, Z. Y. Wang, M.C. Li, M.Y. Yang, H. Cheng, Z.G. Lu, Bimetallic organic frameworks derived CuNi/carbon nanocomposites as efficient electrocatalysts for oxygen reduction reaction, *Sci. China Mater.* 60 (2017) 654–663.
- [29] H. An, L. Wu, L. Mandemaker, S. Yang, J. De Ruiter, J. Wijten, J. Janssens, T. Hartman, W. van der Stam, B.M. Weckhuysen, Sub-second time-resolved surface enhanced Raman spectroscopy reveals dynamic CO intermediates during electrochemical CO<sub>2</sub> reduction on copper, *Angew. Chem. Int. Ed.* 60 (2021) 16576–16584.
- [30] Z. Hu, Y. Lu, M. Liu, X. Zhang, J. Cai, Crystalline red phosphorus for selective photocatalytic reduction of CO<sub>2</sub> into CO, *J. Mater. Chem. A* 9 (2021) 338–348.
- [31] L. Li, Z. Hu, J.C. Yu, On-demand synthesis of H<sub>2</sub>O<sub>2</sub> by water oxidation for sustainable resource production and organic pollutant degradation, *Angew. Chem. Int. Ed.* 59 (2020) 20538–20544.
- [32] Z.F. Hu, J.B. Gong, Z. Ye, Y. Liu, X.D. Xiao, J.C. Yu, Cu(In,Ga)Se<sub>2</sub> for selective and efficient photoelectrochemical conversion of CO<sub>2</sub> into CO, *J. Catal.* 384 (2020) 88–95.
- [33] Z. Hu, W. Liu, Conversion of biomasses and copper into catalysts for photocatalytic CO<sub>2</sub> reduction, *ACS Appl. Mater. Interfaces* 12 (2020) 51366–51373.
- [34] Y. Lan, G. Niu, F. Wang, D. Cui, Z. Hu, SnO<sub>2</sub>-modified two-dimensional CuO for enhanced electrochemical reduction of CO<sub>2</sub> to C<sub>2</sub>H<sub>4</sub>, *ACS Appl. Mater. Interfaces* 12 (2020) 36128–36136.
- [35] F. Bachhuber, J. von Appen, R. Dronskowski, P. Schmidt, T. Nilges, A. Pfizner, R. Wehrich, Van der Waals interactions in selected allotropes of phosphorus, *Z. Fur Krist. Cryst. Mater.* 230 (2015) 107–115.
- [36] H. Ning, X. Wang, W. Wang, Q. Mao, Z. Yang, Q. Zhao, Y. Song, M. Wu, Cubic Cu<sub>2</sub>O on nitrogen-doped carbon shells for electrocatalytic CO<sub>2</sub> reduction to C<sub>2</sub>H<sub>4</sub>, *Carbon* 146 (2019) 218–223.
- [37] D. Zhong, Z.J. Zhao, Q. Zhao, D. Cheng, B. Liu, G. Zhang, W. Deng, H. Dong, L. Zhang, J. Li, J. Li, J. Gong, Coupling of Cu(100) and (110) facets promotes carbon dioxide conversion to hydrocarbons and alcohols, *Angew. Chem. Int. Ed.* 60 (2021) 4879–4885.
- [38] A.J. Garza, A.T. Bell, M. Head-Gordon, Mechanism of CO<sub>2</sub> reduction at copper surfaces: pathways to C<sub>2</sub> products, *ACS Catal.* 8 (2018) 1490–1499.
- [39] D. Li, T. Liu, Z. Yan, L. Zhen, J. Liu, J. Wu, Y. Feng, MOF-derived Cu<sub>2</sub>O/Cu nanospheres anchored in nitrogen-doped hollow porous carbon framework for increasing the selectivity and activity of electrochemical CO<sub>2</sub>-to-formate conversion, *ACS Appl. Mater. Interfaces* 12 (2020) 7030–7037.
- [40] A. Herzog, A. Bergmann, H.S. Jeon, J. Timoshenko, S. Kühl, C. Rettenmaier, M. Lopez Luna, F.T. Haase, B. Roldan Cuenya, Operando investigation of Ag-decorated Cu<sub>2</sub>O nanocube catalysts with enhanced CO<sub>2</sub> electroreduction toward liquid products, *Angew. Chem. Int. Ed.* 60 (2021) 7426–7435.
- [41] Y. Lan, G. Niu, F. Wang, D. Cui, Z. Hu, SnO<sub>2</sub>-modified two-dimensional CuO for enhanced electrochemical reduction of CO<sub>2</sub> to C<sub>2</sub>H<sub>4</sub>, *ACS Appl. Mater. Interfaces* 12 (2020) 36128–36136.
- [42] Y. Lum, J.W. Ager, Stability of residual oxides in oxide-derived copper catalysts for electrochemical CO<sub>2</sub> reduction investigated with <sup>18</sup>O labeling, *Angew. Chem. Int. Ed.* 57 (2018) 551–554.
- [43] Z. Gu, N. Yang, P. Han, M. Kuang, B. Mei, Z. Jiang, J. Zhong, L. Li, G. Zheng, Oxygen vacancy tuning toward efficient electrocatalytic CO<sub>2</sub> reduction to C<sub>2</sub>H<sub>4</sub>, *Small Methods* 3 (2019), 1800449.
- [44] Z. Wang, W. Wang, L. Zhang, D. Jiang, Surface oxygen vacancies on Co<sub>3</sub>O<sub>4</sub> mediated catalytic formaldehyde oxidation at room temperature, *Catal. Sci. Technol.* 6 (2016) 3845–3853.
- [45] Z.-Q. Liang, T.-T. Zhuang, A. Seifitokaldani, J. Li, C.-W. Huang, C.-S. Tan, Y. Li, P. De Luna, C.T. Dinh, Y. Hu, Q. Xiao, P.-L. Hsieh, Y. Wang, F. Li, R. Quintero-Bermudez, Y. Zhou, P. Chen, Y. Pang, S.-C. Lo, L.-J. Chen, H. Tan, Z. Xu, S. Zhao, D. Sinton, E.H. Sargent, Copper-on-nitride enhances the stable electrosynthesis of multi-carbon products from CO<sub>2</sub>, *Nat. Commun.* 9 (2018) 3828.
- [46] H. Gao, L. Sun, M. Li, W. Zhan, X. Wang, X. Han, Fabricating a hollow cuboctahedral structure for N-doped carbon coated p-n heterojunctions towards high-performance photocatalytic organic transformation, *Nano Res.* (2021) 1–8.
- [47] S. Yi, X. Qin, C. Liang, J. Li, R. Rajagopalan, Z. Zhang, J. Song, Y. Tang, F. Cheng, H. Wang, M. Shao, Insights into KMnO<sub>4</sub> etched N-rich carbon nanotubes as advanced electrocatalysts for Zn-air batteries, *Appl. Catal. B: Environ.* 264 (2020), 118537.
- [48] W. Liu, Z. Lang, The structure and self-regeneration performance of Salix psammophila-activated carbon modified by Ag and N co-doped TiO<sub>2</sub>, *RSC Adv.* 10 (2020) 3844–3852.
- [49] J. Sun, N. Guo, Z. Shao, K. Huang, Y. Li, F. He, Q. Wang, A facile strategy to construct amorphous spinel-based electrocatalysts with massive oxygen vacancies using ionic liquid dopant, *Adv. Energy Mater.* 8 (2018), 1800980.
- [50] Q. Gan, N. Qin, S. Gu, Z. Wang, Z. Li, K. Liao, K. Zhang, L. Lu, Z. Xu, Z. Lu, Extra sodiation sites in hard carbon for high performance sodium ion batteries, *Small Methods* 5 (2021), 2100580.
- [51] Y. Zhang, Z. Xu, Q. Wang, W. Hao, X. Zhai, X. Fei, X. Huang, Y. Bi, Unveiling the activity origin of ultrathin BiOCl nanosheets for photocatalytic CO<sub>2</sub> reduction, *Appl. Catal. B: Environ.* 299 (2021), 120679.
- [52] F. Li, X. Yue, D. Zhang, J. Fan, Q. Xiang, Targeted regulation of exciton dissociation in graphitic carbon nitride by vacancy modification for efficient photocatalytic CO<sub>2</sub> reduction, *Appl. Catal. B: Environ.* 292 (2021), 120179.
- [53] Y. Zhao, X. Chang, A.S. Malkani, X. Yang, L. Thompson, F. Jiao, B. Xu, Speciation of Cu surfaces during the electrochemical CO reduction reaction, *J. Am. Chem. Soc.* 142 (2020) 9735–9743.
- [54] Y. Hori, C.G. Vayenas, R.E. White, M.E. Gamboa-Aldeco, *Modern Aspects of Electrochemistry*, (2008), 103.
- [55] S. Zhang, P. Kang, S. Ubnoske, M.K. Brennaman, N. Song, R.L. House, J.T. Glass, T. J. Meyer, Polyethylenimine-enhanced electrocatalytic reduction of CO<sub>2</sub> to formate at nitrogen-doped carbon nanomaterials, *J. Am. Chem. Soc.* 136 (2014) 7845–7848.
- [56] E. Gileadi, *Electrode Kinetics for Chemists, Engineers, and Materials Scientists*, Wiley-VCH, Weinheim, 1993.
- [57] N.G.M. Gattrell, A. Co, J. Electroanal. Chem. Commun. 1 (2006) 594.
- [58] F. Li, L. Chen, G.P. Knowles, D.R. MacFarlane, J. Zhang, Hierarchical mesoporous SnO<sub>2</sub> nanosheets on carbon cloth: a robust and flexible electrocatalyst for CO<sub>2</sub> reduction with high efficiency and selectivity, *Angew. Chem. Int. Ed.* 56 (2017) 505–509.
- [59] Y. Deng, Y. Huang, D. Ren, A.D. Handoko, Z.W. Seh, P. Hirunsit, B.S. Yeo, On the role of sulfur for the selective electrochemical reduction of CO<sub>2</sub> to formate on CuS<sub>x</sub> catalysts, *ACS Appl. Mater. Interfaces* 10 (2018) 28572–28581.
- [60] P.P. Yang, X.L. Zhang, F.Y. Gao, Y.R. Zheng, Z.Z. Niu, X. Yu, R. Liu, Z.Z. Wu, S. Qin, L.P. Chi, Y. Duan, T. Ma, X.S. Zheng, J.F. Zhu, H.J. Wang, M.R. Gao, S.H. Yu, Protecting copper oxidation state via intermediate confinement for selective CO<sub>2</sub> electroreduction to C<sub>2+</sub> fuels, *J. Am. Chem. Soc.* 142 (2020) 6400–6408.
- [61] S. Jiang, K. Klingan, C. Pasquini, H. Dau, New aspects of operando Raman spectroscopy applied to electrochemical CO<sub>2</sub> reduction on Cu foams, *J. Chem. Phys.* 150 (2019), 041718.
- [62] I.V. Chernyshova, P. Somasundaran, S. Ponnurangam, On the origin of the elusive first intermediate of CO<sub>2</sub> electroreduction, *Proc. Natl. Acad. Sci. USA* 115 (2018), E9261.
- [63] S. Zhu, B. Jiang, W.B. Cai, M. Shao, Direct observation on reaction intermediates and the role of bicarbonate anions in CO<sub>2</sub> electrochemical reduction reaction on Cu surfaces, *J. Am. Chem. Soc.* 139 (2017) 15664–15667.
- [64] J. Gao, H. Zhang, X. Guo, J. Luo, S.M. Zakeeruddin, D. Ren, M. Gratzel, Selective C-C coupling in carbon dioxide electroreduction via efficient spillover of intermediates as supported by operando Raman spectroscopy, *J. Am. Chem. Soc.* 141 (2019) 18704–18714.
- [65] I. Oda, H. Ogasawara, M. Ito, Carbon monoxide adsorption on copper and silver electrodes during carbon dioxide electroreduction studied by infrared reflection absorption spectroscopy and surface-enhanced Raman spectroscopy, *Langmuir* 12 (1996) 1094–1097.
- [66] X. Chen, J. Chen, N.M. Alghoraibi, D.A. Henckel, R. Zhang, U.O. Nwabara, K. E. Madsen, P.J.A. Kenis, S.C. Zimmerman, A.A. Gewirth, Electrochemical CO<sub>2</sub>-to-ethylene conversion on polyamine-incorporated Cu electrodes, *Nat. Catal.* 4 (2020) 20–27.
- [67] Y.-B. Chang, C. Zhang, X.-L. Lu, W. Zhang, T.-B. Lu, Graphdiyne enables ultrafine Cu nanoparticles to selectively reduce CO<sub>2</sub> to C<sub>2+</sub> products, *Nano Res.* 15 (2022) 195–201.